Materials and Design 204 (2021) 109665

Contents lists available at ScienceDirect

Materials and Design

journal homepage: www.elsevier.com/locate/matdes

Grain refinement of Fe–Ti alloys fabricated by laser powder bed fusion

Hideaki Ikehata [a,*], David Mayweg [a], Eric Jägle [a,b]

[a] Max-Planck-Institut für Eisenforschung, Max-Planck-Strasse 1, 40237 Düsseldorf, Germany
[b] Universität der Bundeswehr München, Werner-Heisenberg-Weg 39, 85579 Neubiberg, Germany

HIGHLIGHTS

- Samples of Fe-Ti model alloys were produced by Laser Powder Bed Fusion under Ar and N_2 atmosphere.
- A transition from a microstructure containing coarse columnar grains to a refined microstructure with equiaxed grains was confirmed.
- Cubic Ti(O,N) particles with the Baker-Nutting orientation relationship realize grain refinement by heterogeneous nucleation.

GRAPHICAL ABSTRACT

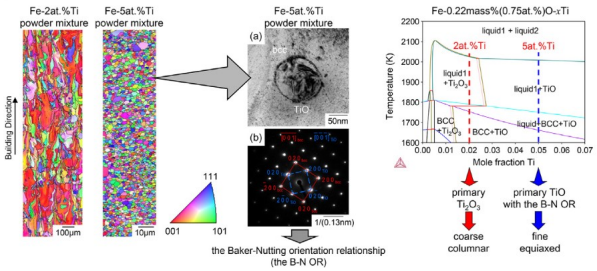

ARTICLE INFO

Article history:
Received 22 December 2020
Received in revised form 24 February 2021
Accepted 15 March 2021
Available online 19 March 2021

Keywords:
Grain refinement
Laser powder bed fusion
Inoculation
Heterogeneous nucleation
Columnar-to-equiaxed transition
The Baker-Nutting orientation relationship

ABSTRACT

Grain structure control is essential in metal additive manufacturing. It is used to avoid anisotropic mechanical properties, hot cracking and to increase the strength via the Hall-Petch effect. Here we demonstrate the use of grain refining particles for grain control in ferritic alloys, specifically Fe-Ti model alloys. We introduce the particles in three different ways, namely (i) by using oxygen-rich raw powders, (ii) by reaction of the molten material with the process gas atmosphere and (iii) by direct addition of the refining ceramic phase in powder form. Samples are produced by Laser Powder Bed Fusion with various concentrations of Ti and under Ar and N_2 atmosphere. The resulting microstructures are analyzed using optical and electron microscopy. We demonstrate a transition from a microstructure containing columnar grains >100 μm in length to a strongly grain refined microstructure with equiaxed grains of approx. 1 μm in size. The refining sub-micron-sized particles in all cases are cubic Ti(O,N). We discuss the findings in the light of thermodynamic calculations as well as established grain refinement models.

1. Introduction

The laser powder bed fusion (LPBF) process is one of the additive manufacturing (AM) processes and is applied for various industrial purposes, such as the production of aerospace parts, casting dies, and biomedical applications. It has been reported that the LBPF process realizes different microstructures than conventional casting, forging, or sintering processes because of the unique thermal history [1]. The microstructure can consist of fine grains and precipitates induced by rapid solidification [2–4], but may also include coarse columnar grains [5–7]. Epitaxial growth was confirmed for many alloys such as Ni superalloys [6], an oxide dispersion strengthened steel [8], and pure tantalum [9]. Many results suggested that the microstructure evolution during AM was affected by both experimental conditions and the chemical composition. Microstructure control is one of the important issues to develop materials for the LPBF process because high (mechanical) performance is often required of parts fabricated by this process.

* Corresponding author.
E-mail addresses: ikehata@mosk.tytlabs.co.jp (H. Ikehata), d.mayweg@mpie.de (D. Mayweg), eric.jaegle@unibw.de (E. Jägle).

https://doi.org/10.1016/j.matdes.2021.109665

Samples fabricated by LPBF can achieve comparable strength to conventionally-processed ones, when optimized process parameters are used. However, mechanical properties such as ductility and fracture toughness must still be improved. The poor values of these properties are usually caused by defects such as voids and/or by a coarse grain structure. One important mechanism to improve the mechanical properties is grain refinement of the matrix, as the mean free path of dislocations is thus reduced. Additionally, grain refinement can also prevent hot cracking during LPBF [2,3]. Nucleation of grains during cooling from the liquid plays an essential role in determining the final grain size distribution, especially if the material does not have a solid-state phase transformation, i.e., when grain refinement by thermo(−mechanical) treatments is not available. Therefore, grain refinement during the solidification is a vitally important mechanism to improve alloys to be used in the LPBF process.

There have been several different methods employed successfully in the literature to control the microstructure, which we will briefly review here. First, by tuning laser process parameters (e.g., energy density [10–14] scanning strategy [10,14–17] laser beam shape [18,19], laser beam diameter [20]), the columnar-to-equiaxed transition during solidification has been achieved. For example, Yang et al. [10] studied the effects of base plate temperature on the microstructural evolution of Al-Mg-Zr alloys and revealed that columnar and equiaxed grains were controllable by these conditions. Several groups modified their laser scanning strategies to control microstructure formation, e.g., Wan et al. in Ni superalloys [15] and AlMangour et al. [16] in austenitic stainless steel. Dehoff et al. realized a desired distribution of columnar and equiaxed grains by the combination of line and spot beam strategies [14]. Another important parameter controlling the final grain size distribution is the energy density of the applied laser [10–13]. Liu et al. calculated the temperature distribution during LPBF by finite element analysis and predicted the microstructure of AlSi10Mg alloy [13]. Shi et al. reported that the shift from a circular Gaussian beam to an elliptical beam profile changed the melt pool size and thus the grain shapes [18]. McLouth studied the promotion of grain coarsening and texturing of superalloys by defocusing the laser beam [20]. Lee et al. evaluated temporal variations of temperature distributions and achieved local microstructure control by applying a primary and secondary beam [21]. Controlling solidification supercooling by remelting every layer twice also promotes grain refinement, for example in Mg alloys [22] and other alloys [23,24].

The commonality of all of these studies is that grain refinement is accomplished by the columnar to equiaxed transition (CET), which is affected by the relation between thermal gradient and interfacial velocity of a liquid/solid interface. Control of these variables requires precise management of the thermal conditions during solidification, which is difficult to achieve in industrially-relevant parts, such as geometrically complex parts resulting from topology optimization. This is due to the heat accumulation in regions of the part when heat conduction away from the part being built is less effective than heat input from the laser [25]. Therefore, a more practical approach to microstructure control via grain refinement is required.

Several new alloys have been investigated to promote grain refinement during LPBF and directed energy deposition processes [26]. Montero-Sistiaga et al. added Si to Al7075 alloy and realized fine grains [27]. The formation of a eutectic microstructure by increasing Cu content also refined Ti-alloys [28]. The addition of Zr to Al alloys also promoted grain refinement and prevented hot cracking [2,3,29]. Martin et al. investigated the grain refinement behavior of pure Al and Al alloys by adding nanoparticles of ceramics and alloying elements [30,31]. They showed that the addition of Al_3X (X = Zr, Nb, Ta) nuclei realized fine equiaxed grains. Grain refinement of the prior β grain of Ti-6Al-4V alloy by adding Y and remelting was attributed to the constitutional supercooling and the formation of Y_2O_3 particles [23]. Bermingham et al. confirmed that the addition of La oxide powder to Ti alloys showed a tendency to transition from columnar grains to equiaxed grains [32]. AlMangour et al. reported a similar grain refinement behavior for an austenite stainless steel by the addition of titanium carbide particles [16].

This brief overview shows that inoculation by grain refining particles is an effective method of producing fine, equiaxed grains in many alloys. It can also be applied to ferritic steels. In our previous work, we could confirm that the addition of TiN powder realized grain refinement of Fe-2at.%Ti and Fe-10at.%Al ferritic steels [33]. Refined microstructures have also been observed recently by other researchers in LPBF-produced ferritic stainless steel [34,35]. Ti(N,O) particles were formed in the liquid phase and became nucleation sites for ferrite. Thus, heterogeneous nucleation is a proven method for grain refinement in LPBF.

This is not unexpected, since TiN particles have been used before as an inoculant for ferritic steels in conventional cast processing, as reviewed by Park et al. [36]. The formation of TiN by Ti inoculant was also effective for grain refinement of ferritic stainless steels during welding processes [37,38]. The dispersion of (Ti,Nb)C, which is of the same crystal structure as TiN (NaCl type structure), also realized grain refinement for microalloyed (ferritic) steels [39].

In this paper, we studied grain refinement in Fe–Ti ferritic steels through the formation of fine particles by in-situ reactions of liquid metal and gaseous elements by heterogenous nucleations of a matrix. Fe–Ti alloys were chosen because Ti is one of the ferrite-stabilizer elements and has a strong affinity for O and N, resulting in forming ceramic particles. We prepared powder mixtures using pure Fe and Ti powders to investigate Ti contents' effect on microstructures. Because the Fe powder contained relatively high amounts of O, the formation of Ti oxides was expected. We also performed the LPBF tests using Fe–Ti atomized powder with low O and N contents to evaluate microstructural differences caused by the building atmosphere. LPBF builds under N_2 atmosphere were conducted to promote TiN particle formation as nucleation sites through Ti and N_2 reaction. Additionally, we prepared Fe–Ti powder mixtures adding TiN particles to clarify the influence of the particle origins, i.e., in-situ formation and pre-mixing of the particles. Microstructure analysis was conducted to investigate the distribution of grains and ceramic particles. Additionally, particle formation was assessed by thermodynamic calculations. A preliminary analysis of the effects of the grain refinement on mechanical properties was performed by Vickers hardness tests.

2. Experimental procedures

2.1. Powder preparations

For LPBF experiments, we prepared several raw powders and powder blends to compare the effect of Ti, O, and N contents and in-situ and ex-situ formation of particles on microstructures. Gas-atomized, spherical, pure Fe, and Ti powders were purchased (powder supplier: TLS Technik GmbH, Germany). The mean powder sizes are 32.95 μm and 25.15 μm, the O contents of both powders are 0.39 mass% and 0.09 mass%, and the N contents are 0.013 mass% and 0.005 mass%, respectively, as measured by hot carrier gas extraction. Due to the high O content in Fe powder, and high O affinity of Ti, in-situ formation of Ti oxide is expected during solidification. Powder mixtures of Fe-2at.% Ti, Fe-5at.%Ti, and Fe-7.5at.%Ti were prepared by mixing the raw powders for 1 h by a tumble mixing machine (WAB AG, Switzerland) at a rate of 30 rpm. Fig. 1 shows the phase diagram of the Fe–Ti binary system calculated by the software Thermo-Calc (database TCFE9). According to the diagram, ferrite is expected as a primary phase, followed (under prevailing non-equilibrium solidification conditions) by the eutectic solidification of ferrite and laves phase (Fe_2Ti). No ferrite-to-austenite transformation is expected.

Alloyed Fe-5.3at.%Ti powder produced by gas atomizing (Nanoval GmbH, Germany) was also used in the experiments. The average diameter of the powder is 24.0 μm. It was determined that the powder contains 0.038 mass% O, and N below the detection limit (<0.005 mass%).

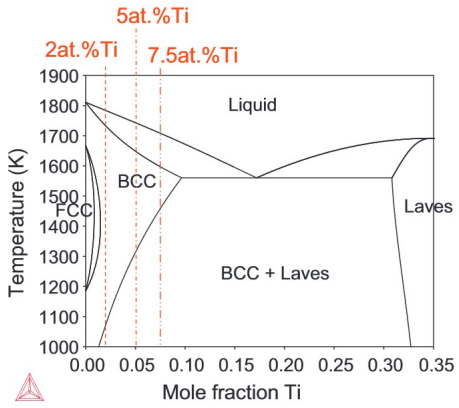

Fig. 1. Calculated phase diagram of Fe—Ti binary system. No solid-state transformation is expected for any of the tested alloys.

Thus, the effect of O and N contents of the raw powders can be investigated by comparing the powder mixtures with the atomized powder. Additionally, the reaction of the alloying elements with the gas atmosphere is expected to become more crucial for the alloyed powder.

Additionally, pre-mixed powder blends were also prepared, including additional TiN powder (Japan New Metal Co., Ltd., Japan) having an average diameter of 2.33 μm. TiN powder of 0.5 or 2 vol% was added to the Fe-2at.%Ti powder mixture and mixed to obtain a uniform distribution of TiN particles by the same condition as the Fe–Ti powder mixtures. It is to be noted that the TiN powder contains a relatively high O content (1.24 mass%) because of the finer particle size compared to the other raw metal powders. Because TiN is a high melting point material, the addition of TiN is expected to result in ex-situ-formed TiN particles in the microstructure after LPBF.

As shown in Table 1, the samples built using the powder mixtures and the alloyed powder will be called mixture samples (*x*Ti-mix-N2 and *x*Ti-mix-Ar; $x = 2, 5, 7.5$) and the alloyed samples (5Ti-alloyed-N2 and 5Ti-alloyed-Ar) in this paper, respectively. Here, "Ar" and "N2" refer to the process atmosphere during the LPBF process. The samples with the addition of the TiN particles are categorized as TiN added samples (*x*TiN-mix-N2; $x = 0.5, 2$).

Mixing pure element powders to realize various chemical compositions and the benefits for material research for LPBF were recently demonstrated by Aota et al. [40]. The addition of the commercial TiN powder realizes flexible control of TiN amount without specially prepared powders (e.g., by atomizing, adding nanoparticles [30,31], powder coating). Although adding fine particles deteriorates powder flowability, the powder mixtures for the TiN added samples were still acceptable for the LPBF experiments.

2.2. LPBF conditions

LPBF experiments were performed by an Aconity3D Mini (Aconity3D GmbH, Germany). The process parameters and the corresponding labels are listed in Table 1. The laser was defocused to 200 μm beam diameter from the standard diameter (90 μm) to form a larger melt pool and realize a homogeneous chemical distribution for the powder mixtures [40]. The energy density E was calculated by the following equation:

$$E = \frac{P}{dvh} \tag{1}$$

where P is the laser power, d is the laser spot diameter, v is the scanning speed, and h is the layer height. Cubic samples of $8 \times 8 \times 10$ mm were produced with the scanning direction rotated 90° between layers. All powder mixtures and the alloyed powder were dried at 100 °C for 1 h prior to the LPBF experiments. The experiments were performed under Ar or N_2 atmosphere. The TiN added samples were built only under N_2 atmosphere to prevent the formation of N_2 gas by decomposition of TiN ($TiN \rightarrow Ti + 1/2\ N_2$) during melting. Additionally, the fine TiN powder contains 1.24 mass% O, which means that the formation of particles (Ti oxides) cannot be avoided even for experiments under Ar atmosphere. Thus, experiments under Ar atmosphere were omitted for the TiN added samples.

2.3. Microstructure and chemical composition analyses

Built samples were cut along the building direction (BD) and polished for microstructure characterizations. The microstructure observation was carried out by a light optical microscope (LOM) and a Zeiss Sigma (Zeiss AG, Germany) scanning electron microscope (SEM). The specimens were etched by Adler etchant for the LOM observation. Chemical analyses were conducted using energy-dispersive X-ray spectroscopy (EDS). Phase distributions and inverse pole figure (IPF) maps were obtained by electron backscattered diffraction (EBSD)).

The distributions of dispersed particles were obtained by analyzing the SEM images. The cross-section images were binarized (manual thresholding), and volume fraction and average diameter were measured by Image-J software. More than 5 images were investigated for each sample.

A thin foil sample for transmission electron microscopy (TEM) analysis was prepared using an FEI Helios NanoLab 600 (FEI Company, USA) dual beam focused ion beam (FIB)-SEM. TEM analyses were conducted on a JEM-F2200FS (JEOL Ltd., Japan) at 200 kV.

The chemical compositions of four samples with the chemical composition of Fe-5at.%Ti (5Ti-mix-N2/Ar and 5Ti-alloyed-N2/Ar) were analyzed by inductively coupled plasma optical emission spectroscopy (ICP-OES) to compare the difference of Ti, O, and N contents for different raw powders (the powder mixture or the alloyed powder) and experimental atmospheres (N_2 or Ar).

Table 1
Nominal chemical compositions and experimental conditions.

Composition	Label	Powder type	Beam diameter μm	Laser power W	Scan speed mm/s	Hatch space μm	Layer height μm	Energy density J/mm^3	Atmosphere
Fe-2at.%Ti	2Ti-mix-N2	mixture	200	360	600	75	40	75	N_2
Fe-5at.%Ti	5Ti-mix-N2	mixture							N_2
Fe-5at.%Ti	5Ti-mix-Ar	mixture							Ar
Fe-5at.%Ti	5Ti-alloyed-N2	alloyed							N_2
Fe-5at.%Ti	5Ti-alloyed-Ar	alloyed							Ar
Fe-7.5at.%Ti	7.5Ti-mix-N2	mixture							Ar
0.5vol%TiN/Fe-2at.%Ti	0.5TiN-mix-N2	mixture							N_2
2vol%TiN/Fe-2at.%Ti	2TiN-mix-N2	mixture							N_2

2.4. Hardness measurement

Vickers hardness testing was carried out with a weight of 9.8 N (1 kgf) on a cross-sectional surface parallel to the BD. The measurements were conducted 5 times for each sample, and the obtained values were averaged.

3. Results

3.1. Microstructures of the raw powders

Fig. 2 shows the backscattered electron images of cross sections of powder particles used for the experiments. The pure Fe, pure Ti, and alloyed Fe-5at.%Ti powders exhibited an almost spherical shape. As shown in Fig. 2 (a), the pure Fe powder contains many fine particles. Judging from EDS analysis results, these are most likely iron oxides. These particles are formed due to a high O content of the powder (0.39 mass%).

Only a few particles were found in the Ti powder and Fe-5at.% alloyed powder, as shown in Fig. 2 (b) and (c). Additionally, the size of the particles in these powders was finer than in the pure Fe powder.

The TiN powder is comprised of partially polygonal or irregular shaped particles, as shown in Fig. 2 (d).

3.2. Microstructures of the matrices

A typical microstructure of the samples fabricated by LPBF contains few pores, as displayed in Fig. 3. The samples were almost fully dense, and only few pores were detected (Fig. 3 (a)), although cracks propagated from the side walls for 7.5Ti-mix-N2 (Fig. 3 (b)). The microstructures of the samples as seen in LOM after Adler etching are displayed in Fig. 4. The melt pool boundaries are visible in the etched microstructures, and are indicated by the white arrows. There are coarse grains and some of which are elongated along the BD (indicated by the black dotted arrows) in the microstructure of 2Ti-mix-N2. On the other hand, it was shown that the grains of 5Ti-mix-N2, 5Ti-mix-Ar, 5Ti-alloyed-N2, and 7.5Ti-mix-N2 are equiaxed and fine. Bimodal microstructures consisting of fine equiaxed and elongated columnar grains are observed for the samples of 5Ti-alloyed-Ar, and 0.5TiN-mix-N2.

Fig. 5 shows higher magnification, backscattered electron (BSE) images of the unetched samples. All the matrices mainly consist of a single-phase and contain fine dark-appearing particles. The average radius and volume fraction of the particles were obtained from image analysis and are displayed in Table 2. Most particles are spherical but some rectangular particles were also found. There were a few relatively large particles (around 1 μm) as well. The comparison between 5Ti-mix-N2 and 5Ti-mix-Ar showed no significant difference in the distribution of the particles caused by the building atmosphere. On the other hand, the alloyed samples (5Ti-alloyed-N2 and 5Ti-alloyed-Ar) show much lower volume fractions of particles. Especially 5Ti-alloyed-Ar showed the minimum volume fraction of 0.34 vol%. Addition of 2 vol% TiN increased the particle volume fractions for 2TiN-mix-N2. The average radii are similar for all samples, around 0.02 μm.

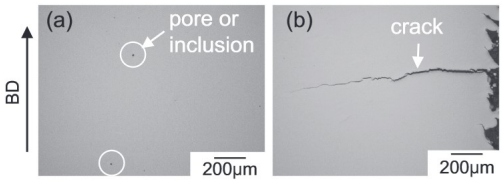

Fig. 3. LOM images of samples without etching. (a) a typical image (5Ti-mix-N2, note few small pores or inclusions were observed), (b) the crack observed in 7.5Ti-mix-N2.

The particles of the TiN added samples (xTiN-mix-N2, $x = 0.5, 2$) are finer than the average sizes of the originally added TiN (2.33 μm) powder. It was also demonstrated that most particles have a more spherical shape (Fig. 5 (g) and (h)) than the irregular shaped ones in the raw powder (Fig. 2 (d)). These results suggest that the TiN powder particles entirely or partially melt during the building process. Grain boundary precipitates are visible in 7.5Ti-mix-N2, as shown in Fig. 5 (f).

3.3. Chemical and grain distribution obtained from EDS and EBSD analysis

Fig. 6 shows the results of the EDS mapping analyses. The chemical distributions of Ti (and Fe) for the mixture samples and TiN added samples (2Ti-mix-N2, 5Ti-mix-N2, 7.5Ti-mix-N2, and 2TiN-mix-N2) are almost homogeneous (Fig. 6 (a), (b), (d), and (e)), although areas with a length of some tens of μm with slight enrichment in Ti were found. These results suggest that the Ti and Fe raw powder were mixed well, and Ti oxide or oxynitride particles were formed during the melting and solidification process. In contrast, 5Ti-alloyed-N2 exhibits completely uniform chemical distribution, as shown in Fig. 6 (c). Thus, the difference of chemical distributions between the mixture samples, the alloyed samples, and the TiN added samples is not significant. The formation of Ti oxide or oxynitride layers at the surface of sample 5Ti-mix-N2 was shown as well in Fig. 6 (f).

Colored IPF maps of the ferrite grains that are parallel to BD and IPFs in the same direction obtained from the EBSD analysis are shown in Fig. 7. The black lines mark grain boundaries (misorientation >10°). The grain shape tendencies (equiaxed, bimodal, or columnar) and the average diameters of the equiaxed grains are summarized in Table 2. The microstructure of the 2Ti-mix-N2 sample show columnar grains elongated along the BD (Fig. 7 (a)). The long axis length of most grains exceeds 100 μm, which is larger than an individual layer thickness (40 μm). Additionally, each grain shows a crystallographic texture of ⟨0 0 1⟩ direction along BD, as shown in Fig. 7 (a). It is well known that the ⟨0 0 1⟩ direction is the easy growth direction for bcc materials during solidification [41]. These results suggested that the grains grew epitaxially from already-solidified material. It should be noted that a small number of equiaxed grains were also found in 2Ti-mix-N2. The matrices

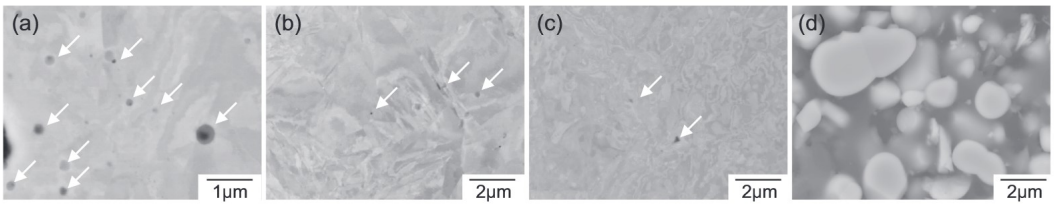

Fig. 2. Cross section SEM images of the raw powders. (a) Pure Fe, (b) pure Ti, (c) alloyed Fe-5at.%Ti, (d) TiN. The white arrows indicated inclusions (oxide particles). Many fine oxide particles can be observed in (a).

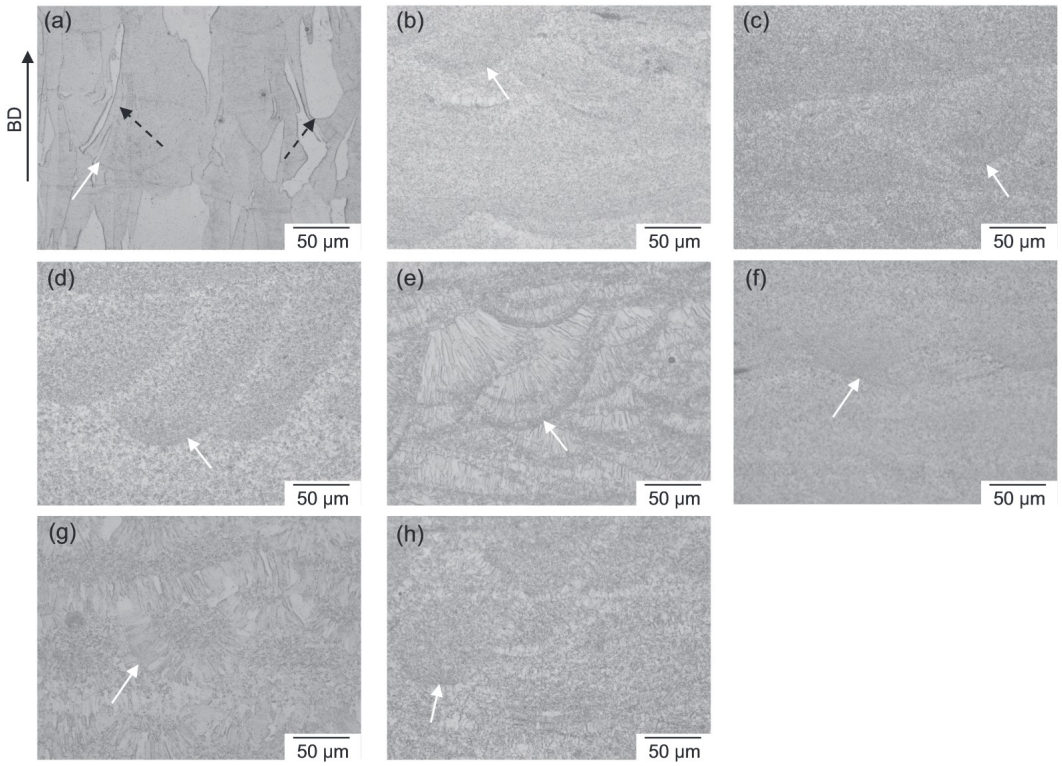

Fig. 4. LOM images of samples after Adler etching. (a) 2Ti-mix-N2, (b) 5Ti-mix-N2, (c) 5Ti-mix-Ar, (d) 5Ti-alloyed-N2, (e) 5Ti-alloyed-Ar, (f) 7.5Ti-mix-N2, (g) 0.5TiN-mix-N2, (h) 2TiN-mix-N2. The melt pool boundaries were confirmed as indicated by the white arrows. The black dotted arrows indicate elongated grains along BD in (a). Coarse columnar grains were observed in (e) and (g).

of 5Ti-mix-N2, 5Ti-mix-Ar, and 7.5Ti-mix-N2 consist of the fully equiaxed grains, as shown in Figs. 5 (b), (c), and (d), whose average diameters are 1.3 μm, 1.5 μm, and 0.85 μm, respectively.

The IPF maps of the alloyed samples showed a clear dependency on the testing atmosphere. The grain distribution of the sample built under N_2 (5Ti-alloyed-N2) was similar to that of 5Ti-mix-N2. The average diameter of the equiaxed grains was 0.80 μm. On the other hand, the grains of 5Ti-alloyed-Ar consist of coarse columnar and fine equiaxed grains. The distribution of the grains was sandwich-like, i.e., the columnar grains are separated by layers of fine grains. The lengths of the columnar grains are less than the layer thickness, meaning they are shorter than those of 2Ti-mix-N2, and the texture of ⟨0 0 1⟩ direction was not found.

In the case of the TiN added samples, the grain size and shape distributions depend on the amount of the TiN powder. The grains showed a bimodal distribution that was similar to that of 2Ti-alloyed-Ar when the amount of TiN is 0.5 vol%. As shown in Fig. 7 (g), the columnar grains elongate radially, which means along the largest thermal gradients during solidification. The columnar grains tend to form from the outer borders of melt pools, consequently, the melt pool boundaries are visible. The addition of 2 vol% of TiN particles decreased the grain sizes and changed to the nearly equiaxed shape. The average diameters of 2TiN-mix-N2 are 1.08 μm.

3.4. Phase analysis of dispersed particles

The phase distributions of the mixture samples obtained from EBSD analysis are shown in Fig. 8 to identify the phases of the dispersed particles. Although due to the limited resolution, the finest particles could not be analyzed, one large particle in 2Ti-mix-N2 was identified having corundum (Al_2O_3) structure (trigonal, space group 167), meaning that the particle is Ti_2O_3 (Fig. 8 (a)). The particles in 5Ti-mix-N2 and 7.5Ti-mix-N2 were indexed as NaCl type crystal structure (cubic, space group 225), as shown in Fig. 8 (b) and (d). The same NaCl type structure precipitations were also confirmed in 5Ti-alloyed-N2 (Fig. 8 (e)) and 2TiN-mix-N2 (Fig. 8 (f)). From a thermodynamics point of view, i.e., taking the phase diagrams (Fig. 13) into account, these particles are estimated to be TiO or TiN.

The orientation relationship between the particle (marked B) and an adjacent ferritic grain (marked A) of the 5Ti-mix-N2 sample shown in Fig. 8 (b) was analyzed. Black lines in Fig. 8 (b) indicate grain and phase boundaries. The rotation direction and angle are approximately [0 1 30] and 44.8°, respectively as illustrated in Fig. 8 (c). This orientation relationship is close to the Baker-Nutting orientation relationship (B–N OR) which is $(0\ 0\ 1)_{ferrite}//(0\ 0\ 1)_{particle}$ and $[1\ 1\ 0]_{ferrite}//[1\ 0\ 0]_{particle}$ [42]. The result of the EBSD mapping also reveals that the phase observed to form along the grain boundaries

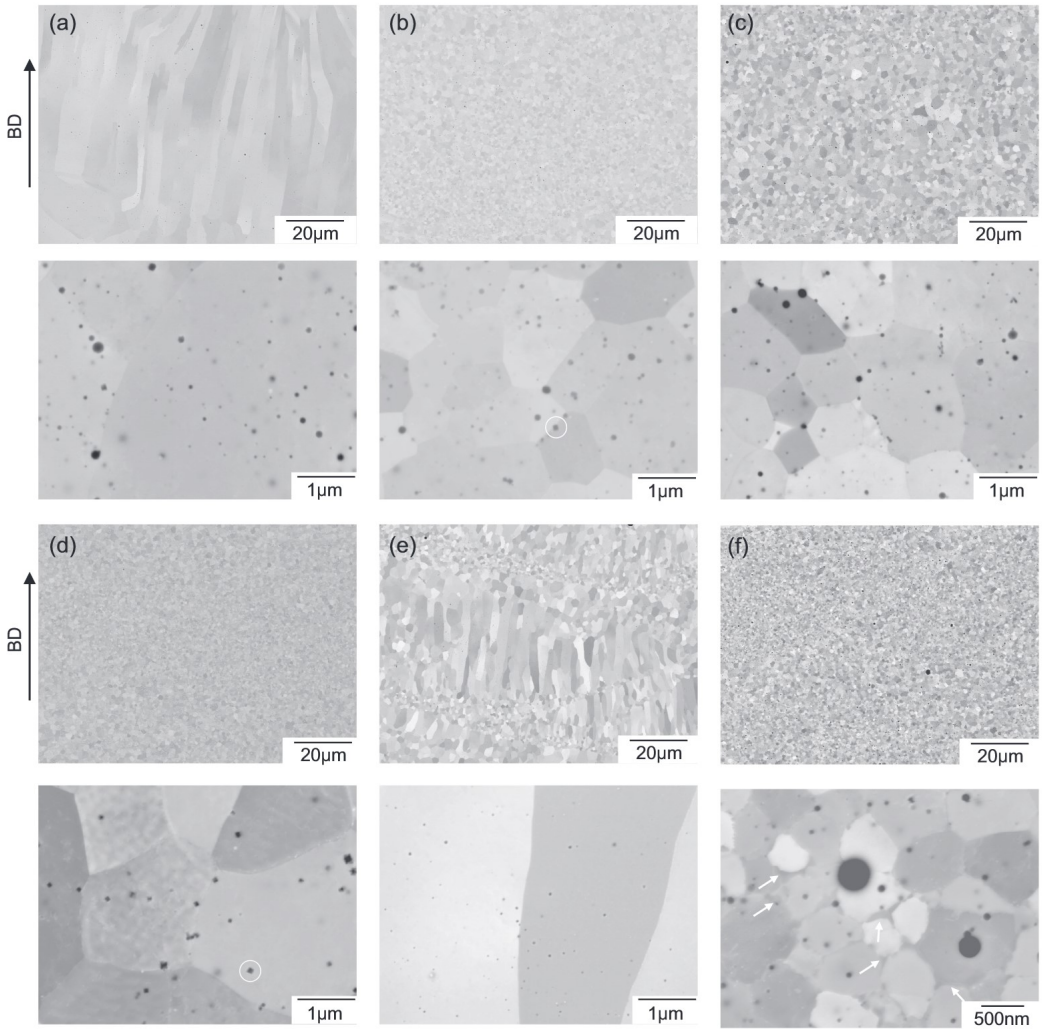

Fig. 5. SEM images of samples without etching. upper images: low magnification, lower images: high magnification. (a) 2Ti-mix-N2, (b) 5Ti-mix-N2, (c) 5Ti-mix-Ar, (d) 5Ti-alloyed-N2, (e) 5Ti-alloyed-Ar, (f) 7.5Ti-mix-N2 (g) 0.5TiN-mix-N2, (h) 2TiN-mix-N2. All samples contain fine particles. Most particles are spherical, but rectangular particles were also found (see white circles). There were grain boundary precipitates in 7.5Ti-mix-N2 as indicated by the white arrows.

in the 7.5Ti-mix-N2 microstructures (Fig. 8 (e)) was the Laves phase (Fe_2Ti). A eutectic structure, e.g., a fine lamellar structure of ferrite and Laves phases, was not found.

3.5. TEM particle analysis

Fig. 9 shows scanning TEM high angle annular dark field images of 5Ti-mix-N2 (Fe-5at.%Ti). Not only the spherical submicron particles, but also nano-size particles are observed. The selected area diffraction SAD pattern of these larger particles reveals a cubic structure. An image of Particle D in Grain C and a SAD pattern of both are displayed in Fig. 10. The EDS analysis of Particle B showed that this particle contains Ti and O. These results suggest that particle D is NaCl type TiO. It was also confirmed that the crystallographic orientation relationship between grain C and particle D is close to B–N OR. The schematic of the relationship is illustrated in Fig. 11. It shall be noted that the Laves phase was observed neither at the grain boundaries nor in the ferrite grains.

3.6. Chemical composition analysis

The chemical compositions of Fe-5at.%Ti samples are displayed in Table 3. A decrease of Ti contents from powder (mixture) to LPBF sample was found for the 5Ti-mix-N2 and 5Ti-mix-Ar, but the alloyed

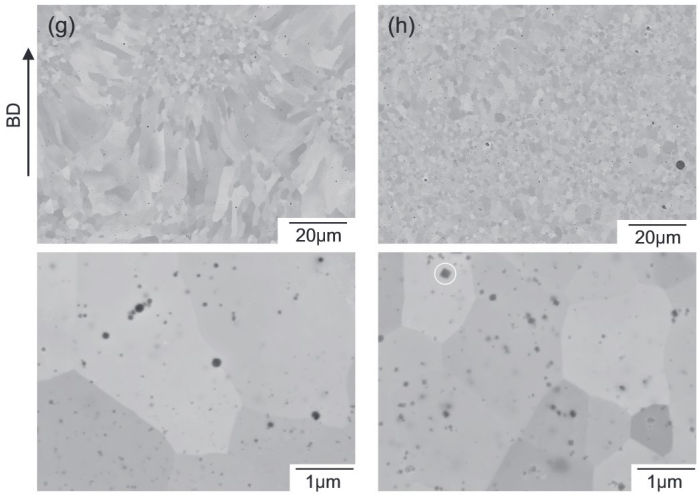

Fig. 5 (*continued*).

samples showed an equivalent Ti content to the raw alloyed powder (5.3 at.%). The O and N contents estimated from the chemical composition of the raw Fe and Ti powders are 0.38 mass% and 0.013 mass%, respectively. The result of 5Ti-mix-N2 reveals a decrease of the O content and an increase of N content compared with the powder mixture. For 5Ti-mix-Ar, the O content decreased as well, but the N content was almost equivalent to the powder mixture.

In the case of the alloyed samples, the O contents are much less than those of the mixture samples. The O contents of 5Ti-alloyed-N2 and 5Ti-alloyed-Ar are 0.050 mass% and 0.055 mass%, which slightly increased from that of the raw powder (0.038 mass%). N content was only detected for 5Ti-alloyed-N2, which was 0.030 mass%.

3.7. Vickers hardness testing

Table 4 shows the results of Vickers hardness tests. The 2Ti-mix-N2 shows the lowest hardness. Hardness increased with the increase of the Ti content for the mixture samples. A similar tendency was found in the TiN added specimens. In the alloyed sample cases, the sample under N_2 atmosphere (5Ti-alloyed-N2) has a higher hardness than that under Ar (5Ti-alloyed-Ar). The addition of TiN particles also increased the hardness.

4. Discussion

4.1. Mechanism of grain refinement

As described in section 3.2, 2Ti-mix-N2 showed coarse columnar grains that are larger than the layer thickness (40 μm) and a texture of ⟨0 0 1⟩ along the BD. In contrast, the samples containing more than 5 at.%Ti formed fine equiaxed grains. The average grain diameters of the latter cases are around 1 μm, so the grain refinement is significant compared with 2Ti-mix-N2. Two samples (5Ti-alloyed-Ar and 0.5TiN-mix-N2) showed bimodal grain distributions. Because no solid-state phase transformation is expected from the phase diagram (Fig. 1), the mechanisms of this grain refinement phenomenon are expected to be stemming from the solidification process. As reviewed in the introduction section, there are several mechanisms that can lead to grain refinement during the solidification of LPBF processes. In this section, we will discuss and exclude these mechanisms one by one and thus support our hypothesis that heterogeneous nucleation is responsible for grain refinement in the current study.

4.1.1. Eutectic solidification mechanism

Montero-Sistiaga et al. created a refined matrix by adding Si to Al7075 alloy [27]. They claimed that the grain refinement was achieved by enhancement of eutectic solidification through Si addition. Fig. 12 shows the Scheil calculation result for Fe-5at.%Ti obtained from Thermo-Calc. According to the Scheil calculation, a eutectic microstructure was predicted following ferrite solidification. Although precipitates of the Laves phase were confirmed at the grain boundaries of 7.5Ti-mix-N2, SEM and TEM measurements did not reveal any eutectic microstructure for Fe-5at.%Ti (Figs. 8 and 9). Thus, we exclude grain refinement by the formation of a eutectic phase.

4.1.2. Laser scanning strategy

It is also well known that laser scanning strategies can affect the microstructures fabricated by LPBF. For example, the phenomenon was shown to take place for a Ni-based superalloy by Wan et al. [15] and in stainless steel with TiC particles by AlMangour [16]. Because the same scanning strategy was applied for all alloys, such mechanisms are not relevant in the present experiments.

4.1.3. CET by the temperature distribution

The relationship between the thermal gradient and velocity of the interface between the melt pool and solid was also proposed as controlling the grain size via the columnar-to-equiaxed transition (CET) [43–45]. According to the theory, the columnar grains are obtained at the conditions of high thermal gradient and low interface velocity. A decrease of the thermal gradient and an increase of the interface velocity results in fully equiaxed grains. Because the amount of Ti altered the grain morphology significantly, we focus on the alloying effect on the alteration in 2Ti-mix-N2 and 5Ti-mix-N2, which showed coarse columnar grains, and fine equiaxed grains, respectively. Therefore, the temperature distributions of these two powder mixture samples were investigated.

The thermal gradient ($G(z,t)$), heating/cooling rate ($R(z,t)$), and the solid-liquid interface velocity ($V(z,t)$) developed by a laser illumination

Table 2
Summaries of microstructure analysis. Dark particle distributions obtained from image analysis and overview of matrix grain shapes and average diameters obtained from the EBSD analysis.

Composition	Label	Dark particle		Matrix	
		Volume fraction %	Average radius μm	Grain shape and size	Average diameter μm
Fe-2at.%Ti	2Ti-mix-N2	1.28	0.015	columnar (epitaxial) + small amount of fine	–
Fe-5at.%Ti	5Ti-mix-N2	1.47	0.019	equiaxed, fine	1.34
Fe-5at.%Ti	5Ti-mix-Ar	1.29	0.015	equiaxed, fine	1.46
Fe-5at.%Ti	5Ti-alloyed-N2	0.60	0.019	equiaxed, fine	1.13
Fe-5at.%Ti	5Ti-alloyed-Ar	0.34	0.012	bimodal: columnar (not epitaxial) + equiaxed	–
Fe-7.5at.%Ti	7.5Ti-mix-N2	1.80	0.024	equiaxed, fine, laves phase	0.85
0.5vol%TiN/Fe-2at.%Ti	0.5TiN-mix-N2	1.33	0.013	bimodal: columnar (not epitaxial) + equiaxed	–
2vol%TiN/Fe-2at.%Ti	2TiN-mix-N2	2.48	0.022	equiaxed, fine	1.20

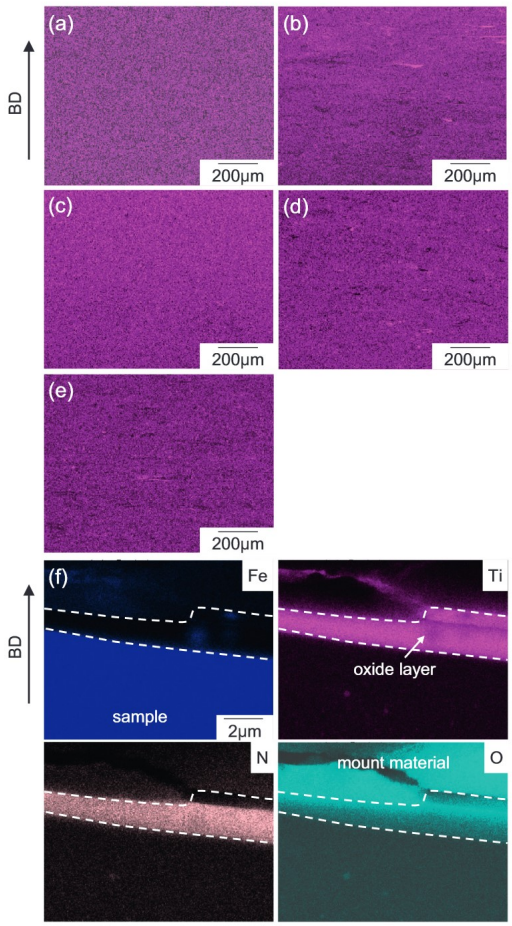

Fig. 6. Chemical distributions of Ti ((a) ~ (e)), and Fe, Ti, N, and O ((f)) obtained from EDS analysis. (a) 2Ti-mix-N2, (b) 5Ti-mix-N2, (c) 5Ti-alloyed-N2, (d) 7.5Ti-mix-N2, (e) 0.5TiN-mix-N2, (f) surface layer of 5Ti-mix-N2. A slight enrichment of Ti was confirmed in (b), (d), and (e), but the distribution of Ti in (a), and (c) is uniform. An oxide layer consisting of Ti oxide was confirmed in (f).

were estimated by equations proposed by Greenwald et al. [46], where z is the depth from the surface, and t is time. The equations, the boundary conditions, and the thermal properties used for the calculation are described in the Appendix. The calculated results are collected in Table 5. It shows that the amount of Ti alloying does not significantly alter the pertinent calculated values. For example, the ratios of the thermal gradients and solid-liquid interface velocities between Fe-2at.%Ti and Fe-5at.%Ti alloys were 1.18 and 0.96, respectively (Table 5). The results suggest that the thermal distributions around the laser spot were practically identical for both samples, so CET was not expected to happen between the two different mixture samples.

4.1.4. Increase of cooling rate by remelting

Increasing the cooling rate and the thermal gradient has been shown by Zhang et al. to be a simple and effective mechanism for grain refinement in remelted Mg and Ti alloys [22,23]. As estimated in subsection 4.1.3, the ratio of the cooling rate of Fe-2at.%Ti and Fe-5at.%Ti alloys is 1.13, i.e., the chemical composition difference does not affect the temperature distribution. Additionally, we do not perform remelting in this study. Therefore, we can exclude this mechanism for grain refinement in this study.

4.1.5. Heterogeneous nucleation mechanism by the formation of grain nuclei

The presence of nuclei during solidification promotes heterogeneous nucleation and results in grain refinement. For example, Zhang et al. found grain refinement in an Al alloy upon adding Zr powder [2]. This grain refinement was the result of the formation of primary Al_3Zr precipitates having a low lattice misfit with the Al matrix, which thus act as ideal nuclei during solidification. The addition of La oxide powder also leads to grain refinement in Ti alloys [32]. The lattice misfit between the oxide and the matrix is an essential factor for grain refinement for both cases. Villaret et al. observed a similar grain refinement for ferritic stainless steel with Ti addition fabricated by a welding process [37,38]. Because many fine particles were found in all of our samples, we expect that grain refinement by heterogeneous nucleation is the operating mechanism in our material. This mechanism will be discussed in the following sections in more detail.

4.2. Grain refinement controlled by adding Ti

The O content of the raw powder of Fe-5at.%Ti mixture is estimated as 0.38 mass% from the O contents of the pure Fe and Ti powders, and most of the O originates from the pure Fe powder. Thus, a reaction between Ti and O is expected to occur, forming compounds that affect the microstructure. The roles of Ti and O can be investigated by comparing the results of the mixture samples with different Ti contents.

Although the O contents of 5Ti-mix-N2 and 5Ti-mix-Ar decrease to around 0.2 mass%, after the fabrication, O contents are high enough to form oxide particles. Thus, the mixture samples are expected to contain a noticeable amount of oxide particles. Fig. 13 shows the phase diagram

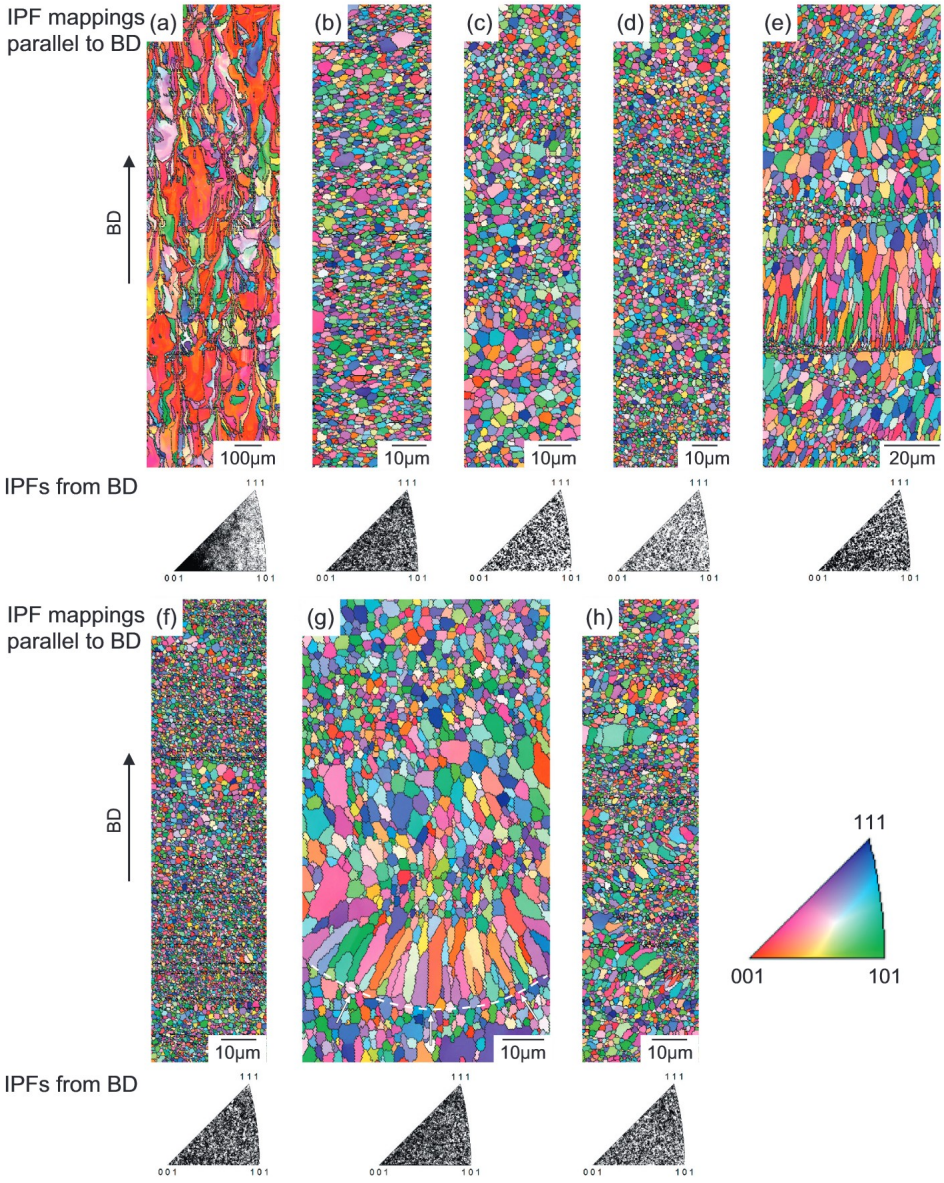

Fig. 7. IPF mappings in the cross section parallel to BD (upper) and IPFs from the BD obtained from EBSD analysis. (a) 2Ti-mix-N2, (b) 5Ti-mix-N2, (c) 5Ti-mix-Ar, (d) 5Ti-alloyed-N2, (e) 5Ti-alloyed-Ar, (f) 7.5Ti-mix-N2, (g) 0.5TiN-mix-N2, (h) 2TiN-mix-N2. Coarse columnar grains can be observed in (a). The microstructures in (e) and (g) are bimodal. The texture of strong ⟨0 0 1⟩ direction along BD was confirmed only in (a). A melt pool trace is visible in (g) as indicated by the white arrow and dotted line.

calculated for (a) Fe-0.2mass%O-*x*Ti system and (b) Fe-0.03mass%N-*x*Ti by Thermo-Calc (using database TCFE9). Because Ti has a high affinity to O, Ti oxides are produced by the reaction between O and Ti atoms as the primary phases at temperatures above the melting point of the alloy, as shown in Fig. 13 (a). The phase diagram suggests that there are three stable Ti oxide phases (TiO_2, Ti_2O_3, and TiO) and that the Ti content controls the phase stability of these oxides. The equilibrium oxide phase around liquidus temperature is TiO_2 for relatively low Ti compositions, and the increase of Ti content changes the equilibrium Ti oxide from Ti_2O_3 to TiO at around 3 at.% Ti, so the primary phases for 2Ti-mix-N2

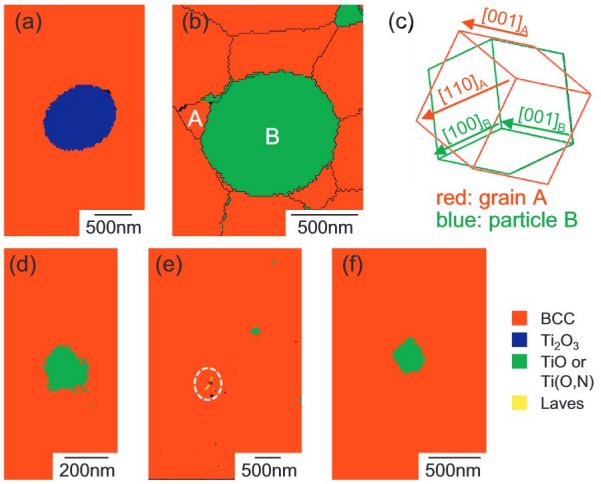

Fig. 8. Precipitated particle phases obtained from EBSD analysis. (a) 2Ti-mix-N2, (b) 5Ti-mix-N2, (c) schematic crystallographic orientation, (d) 5Ti-alloyed-N2, (e) 7.5Ti-mix-N2, (f) 2TiN-mix-N2. The crystal lattices in (c) illustrate that grain A and particle B nearly realize the B–N relationship. note: The black lines in (b) indicate grain and phase boundaries and the white dotted circle in (d) indicates the Lave phase.

(2at.%) and 5Ti-mix-N2 (5at.%) are expected to be Ti_2O_3 and TiO, respectively. Thus, the solidification of ferrite (BCC) starts after solidifying the oxide phases (Ti_2O_3 and TiO), and they possibly become nucleation sites for ferrite. This predicted transition was experimentally confirmed by EBSD analysis, as shown in Fig. 4. Cubic TiO particles were also observed in TEM measurement for Fe-5at.%Ti (Figs. 9 and 10).

From thermodynamic calculations, TiO is the primary oxide phase for the 5Ti-mix-N2, 5Ti-mix-Ar, and 7.5Ti-mix-N2 samples. Therefore, it is essential to know whether TiO can act as a site of heterogeneous nucleation for the ferrite grains. The crystallographic structure of TiO is NaCl, which is the same as TiN, and it has been reported that TiN particles represent excellent nucleation sites for ferrite grains because of the small lattice misfit between TiN and ferrite [47]. The small misfit is present in B–N OR (crystallographic relationships: $(0\,0\,1)_{ferrite}//(0\,0\,1)_{TiN}$ and $[1\,1\,0]_{ferrite}//[1\,0\,0]_{TiN}$). The results from EBSD and TEM measurements suggest that the B–N OR is present during/after solidification in 5Ti-mix-N2.

To become an ideal nucleus for the ferrite grains, the lattice misfit between the particle and the grain should be as small as possible. The misfit ε in the B–N OR was calculated by the following eq. (2) [42];

$$\varepsilon = \frac{2\left(a^{particle} - \sqrt{2}a^{ferrite}\right)}{a^{particle} + \sqrt{2}a^{ferrite}} \quad (2)$$

where $a^{particle}$ and $a^{ferrite}$ are the lattice constants of particle and matrix, respectively. The misfit ε becomes zero when $a^{particle} = \sqrt{2}a^{ferrite}$. The lattice misfits of NaCl type Ti-based particles (e.g., TiN, TiO, and TiC) with the ferritic matrix of Fe-5at.%Ti were calculated by using Thermo-Calc as shown in Fig. 14. The calculated lattice misfits of all particles are almost equivalent (less than 0.06), and the misfit of TiO is even lower than that of the known grain refiner TiN. The low misfit between the matrix and the TiO particle was confirmed by the SAD pattern in Fig. 10 (b). These results indicate that the dispersed particles in 5Ti-mix-N2, 5Ti-mix-Ar, and 7.5Ti-mix-N2 samples have NaCl type crystal structure and with low misfit with the ferrite grains. Thus, we conclude that the particles are heterogeneous nucleation sites and cause the observed grain refinement.

In contrast, Ti_2O_3 forms an incoherent interface with the ferrite matrix, resulting from high misfit strain (~0.25) [48]. As a result, these oxides are not efficient for grain refinement in ferrite. That is the reason why in 2Ti-mix-N2, no grain refinement was observed, and coarse columnar grains formed instead. Thus, the grain refinement was promoted by forming TiO particles that realize the B–N OR with the ferrite grain. The Ti content is crucial to control the stability of TiO, as predicted by the thermodynamic calculation (Fig. 13 (a)).

It should be noted that the reduction of O content from the raw powder mixture (0.38 mass%) is assumed to occur via the formation of oxidized spatters [49,50] and a Ti oxide liquid phase (slag) during the building process as shown in Fig. 6 (f).

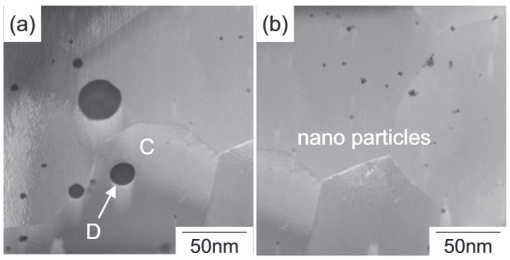

Fig. 9. Overall STEM images of 5Ti-mix-N2. (a) spherical particles, (b) grains containing nano-sized particles.

4.3. Grain refinement controlled by O and N contents

In the case of the alloyed samples, the formation of the grain-refining particles (TiO) does not take place like in the mixture samples because the alloyed raw powder contains a much smaller amount of O. The N contents show a dependency on the gas atmosphere used in LPBF, where N was detected only in the samples built under N_2 (5Ti-mix-N2

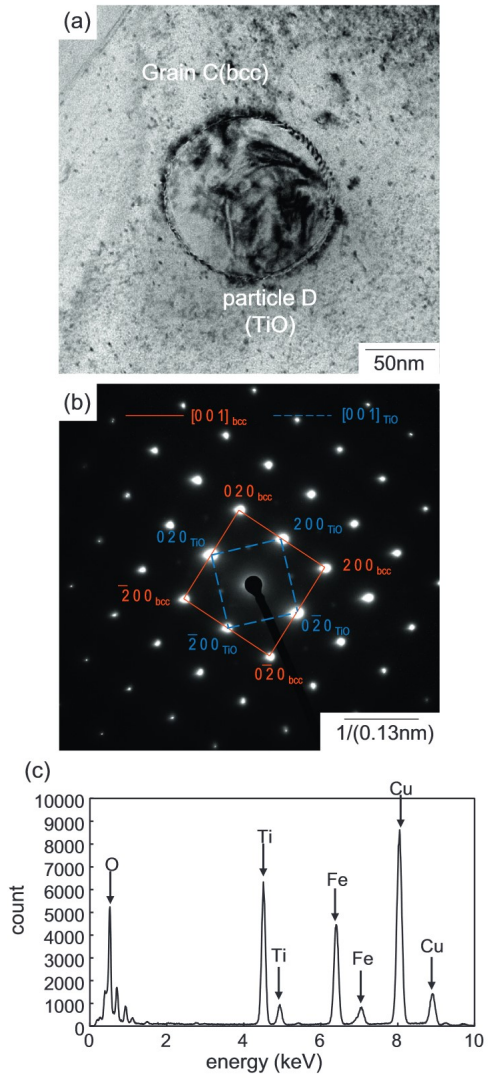

Fig. 10. Results of TEM analysis. (a) TEM image, (b) selected area diffraction pattern of grain C and particle D from ⟨0 0 1⟩ direction, (c) EDS result of particle D. The diffraction pattern shows the near B—N orientation relationship between grain C (bcc) and particle D (TiO). Note: The peaks of Cu were caused from the TEM grid made of Cu.

and 5Ti-alloyed-N2) as shown in Table 3. Thus, the difference of O and N contents is essential to control the microstructure of the alloyed samples.

As shown in Fig. 13 (b), the solubility limit of N in the liquid phase is small, and TiN is the only predicted primary phase. TiN is rapidly stabilized with an increase of Ti content, and the melting point of TiN becomes more than 2100 K for Fe-5at.%Ti. Therefore, the formation of both TiO and TiN is predicted for 5Ti-mix-N2 and 5Ti-alloyed-N2 samples. Because no N content was detected for 5Ti-alloyed-Ar and 5Ti-mix-Ar samples, O and N's roles can be evaluated by comparing these two samples.

The equilibrium TiO and TiN contents at the liquidus temperatures were calculated by Thermo-Calc (database: TCFE9) using the compositions displayed in Table 3. The calculated volume fraction of TiO for 5Ti-alloyed-Ar is 0.52 vol%, which is well below that of 5Ti-mix-Ar (2.1 vol%). These fractions are roughly consistent with the volume fraction obtained by image analysis as listed in Table 2 (0.34 and 1.3 vol%, respectively). Although TiO is the primary phase for both samples, the decrease of TiO particle content results in an insufficient number of heterogeneous nucleation sites. Thus, columnar grains were formed as shown in Fig. 2 (e) and Fig. 3 (e).

O contents of 5Ti-alloyed-N2 and 5Ti-alloyed-Ar are equivalent, so the transition from the binodal grains to the equiaxed grains was caused by the increasing N contents. The increase of N originates from the reaction between the molten metal and the N_2 gas [51,52]. Although the N content is small (0.030 mass%), the calculated phase diagram of Fe-0.03mass%N-*x*Ti alloy (Fig. 13 (b)) suggests the formation of TiN as a primary phase. It should be noted that because TiN has the same NaCl type crystal structure and a similar lattice constant to TiO, the actual composition of the particles is expected to be Ti(O,N) [53]. Thus, the Ti(O,N) particles also promote grain refinement because the low lattice mismatch between the Ti(O,N) particle and the ferritic matrix is expected. Although the database used (TCFE9) cannot evaluate Ti(O,N) directly, estimation of the equilibrium condition of 5Ti-alloyed-N2 was conducted by adding the obtained amounts of TiO and TiN. The increase of N content also led to the formation of the Ti(O,N) particles and hence to an overall increase of particle volume fraction, as expected from the thermodynamic calculations (Table 3). This, in turn, led to the grain refinement in 5Ti-alloyed-N2 (and much less in 5Ti-alloyed-Ar) as shown in Fig. 2 (d), Fig. 3 (d), and Fig. 4. Thus, it is concluded that the 5Ti-mix-N2, 5Ti-mix-Ar, and 5Ti-alloyed-N2 samples have equiaxed grains and nearly equivalent average diameters. This result suggests that NaCl-type TiO and Ti(O,N) particles both work well as grain nuclei for ferritic grains and are crucial for grain refinement.

It should be noted that the equilibrium content of N for Fe-5at.%Ti at the melting temperature under N_2 (at 1 atom) is 0.30 mass%. The measured N contents for 5Ti-mix-N2 and 5Ti-alloyed-N2 are around 0.030 mass%, one order of magnitude less than the equilibrium value. On the other hand, the beam diameter was comparatively large, and the scan speed was slow, resulting in several times remelting of the material volume. The results suggest that, under these process conditions, the reaction between N_2 gas and melt metal was not sufficient to reach the equilibrium condition.

4.4. The grain refinement by the direct addition of TiN particles

As shown in Fig. 7, the results of the TiN added samples suggest that the direct addition of the TiN particles promotes grain refinement of Fe-2at.%Ti alloy. The tendency becomes stronger when the amount of the TiN particles is increased. The samples with 0.5 vol% TiN particles (0.5TiN-mix-N2) showed a bimodal distribution of grain size and morphology, meaning a finer grain distribution than 2Ti-mix-N2. As shown in Fig. 13 (b), the solubility of TiN is relatively small in the liquid phase, so TiN solidifies before ferrite. As mentioned above, TiN is known to be effective in causing grain refinement of ferrite [47]. Although the formation of Ti_2O_3 is predicted at 2 at.%Ti by the phase diagram (Fig. 13 (a)), the addition of TiN particles introduces unmelted TiN particles, which promote grain refinement. Additionally, some TiN particles may melt and cause dissolved N in the melt. This N will lead to re-precipitation of TiN particles during cooling, as shown in Fig. 13 (b). However, because the amount of TiN was not sufficient to achieve a homogenous equiaxed grain morphology, a bimodal grain size and morphology distribution were obtained. This tendency is equivalent to the microstructure of 5Ti-alloyed-Ar (despite the higher Ti contents of the latter). The formation of some fine grains prevented the epitaxial growth of the

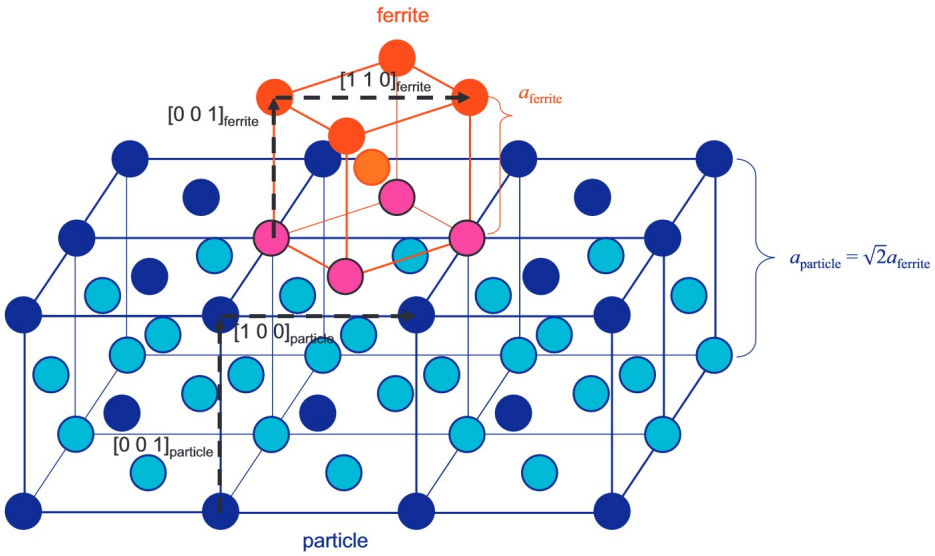

Fig. 11. Schematic of the Baker-Nutting orientation relationship of the ferrite matrix and the NaCl-type particle.

Table 3
Results of chemical composition analysis of LPBF-produced specimens.

Composition	Label	Ti mass% (at.%)	N mass%	O mass%	Volume percent of particles		
					TiN	TiO	Sum
Fe-5at.%Ti	5Ti-mix-N2	3.71 (4.30)	0.030	0.215	0.18	2.00	2.18
Fe-5at.%Ti	5Ti-mix-Ar	3.17 (3.67)	0.006	0.223	0.00	2.10	2.10
Fe-5at.%Ti	5Ti-alloyed-N2	4.68 (5.43)	0.030	0.055	0.20	0.54	0.74
Fe-5at.%Ti	5Ti-alloyed-Ar	4.63 (5.37)	<0.005	0.050	0.00	0.49	0.49

columnar grains across layers. This bimodal microstructure was caused by the temperature distribution around the melt pool, and similar bimodal grain distributions were observed in AlSi10Mg alloy [54].

As shown in Fig. 7 (h), 2TiN-mix-N2 showed fine, equiaxed grains. The addition of 2 vol% of TiN increases the Ti content in the alloy from 2 at.% to 3.2 at.%, resulting in the stabilization of TiO. TiN particles also helped to increase the number of particles by stabilizing the Ti(O,N) phase. That is the reason why the microstructure of 2TiN-mix-N2 appears significantly different from 0.5TiN-mix-N2. Thus, it was confirmed that the direct addition of TiN grain refiner particles is another viable method to achieve grain refinement.

Table 4
Results of Vickers hardness tests.

Composition	Label	Hardness (9.8 N)
Fe-2at.%Ti	2Ti-mix-N2	149.4
Fe-5at.%Ti	5Ti-mix-N2	230.4
Fe-5at.%Ti	5Ti-mix-Ar	207.2
Fe-5at.%Ti	5Ti-alloyed-N2	260.6
Fe-5at.%Ti	5Ti-alloyed-Ar	219.2
Fe-7.5at.%Ti	7.5Ti-mix-N2	297.2
0.5vol%TiN/Fe-2at.%Ti	0.5TiN-mix-N2	167.0
2vol%TiN/Fe-2at.%Ti	2TiN-mix-N2	198.2

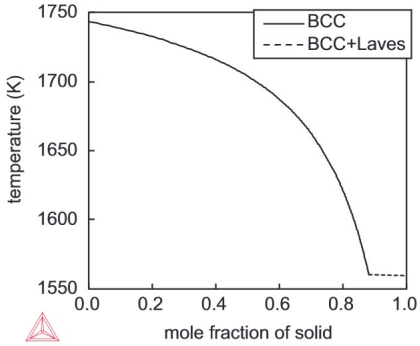

Fig. 12. The result of Scheil calculation by Thermo-Calc for Fe-5at.%Ti alloy. Eutectic solidification is expected at the final stage of solidification.

It should be noted that Ti is required to form TiO particles and to stabilize ferrite, and suppress solid-state transformations (austenite/ferrite) for the samples used in this paper. However, ferritic steels

Table 5
The calculated thermal gradients (G), cooling rates (R), and solid-liquid interface velocities (V). The calculation conditions are shown in Table A-1.

Composition	Thermal gradient, G	Cooling rate, R	Interfacial moving velocity, V
	K/m	K/s	m/s
Fe-2at.%Ti	3.21×10^6	4.08×10^5	0.127
Fe-5at.%Ti	2.72×10^6	3.60×10^5	0.132
Fe-7.5at.%Ti	2.36×10^6	3.24×10^5	0.138

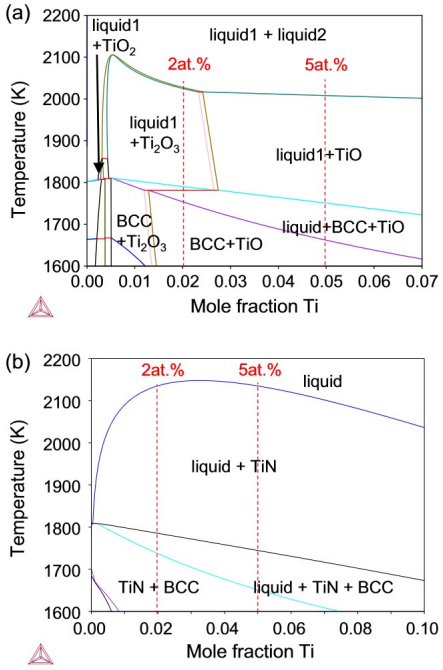

Fig. 13. Calculated phase diagrams of Fe-O-Ti and Fe-N-Ti ternary systems. (a) Fe-0.75 at.% (0.22 mass%)O-xTi, (b) Fe-0.117 at.%(0.03 mass%)N-xTi. It was confirmed in (a) that the primary solidification phases of Fe-2at.%Ti, and 5Ti alloys are Ti_2O_3, and TiO, respectively. In the case of the Fe-N-Ti system, only TiN is expected as the primary phase.

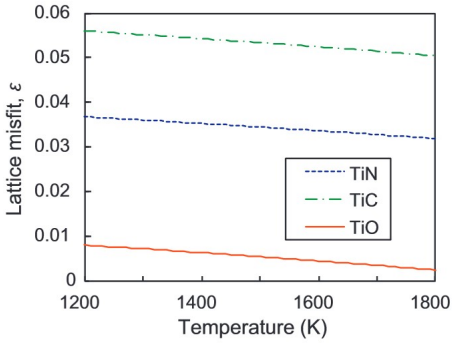

Fig. 14. Calculated lattice misfits of Fe–5Ti alloy with NaCl structured Ti-X ceramic phases. TiC shows the highest lattice misfit of the three phases, but absolute values are still quite low (less than 0.06).

stabilized by other ferrite stabilizing elements (e.g., Si or Al) do not form NaCl-type particles. In these cases, the addition of TiN or TiO particles is expected to be useful for grain refinement. For example, the authors confirmed that Fe-10at.%Al alloy has coarse columnar grains, and the addition of TiN powder triggered the columnar to equiaxed transition and realized grain refinement [33].

4.5. Improvement of hardness by grain refinement

There are several mechanisms that lead to an increase in the hardness of metallic materials, and the activation of several mechanisms is expected for each sample. Here we briefly discuss which strengthening mechanisms are likely to be responsible for the hardness increase in out Fe–Ti samples. The grain size effect is one of the dominant mechanisms (the Hall-Petch law). Solid solution strengthening by substitutional elements (e.g., Ti in Fe) needs to be taken into account, too, even though their strengthening effect is not as high as for interstitial elements. This effect is represented by an increase of the Hall-Petch coefficient and friction stress [55]. Interstitial elements improve the hardness significantly, but such elements (e.g., C, N, and O) tend to be bound in carbides, nitrides, and Ti-oxides in Fe–Ti alloys [56]. Thus, strengthening by interstitial elements does not play a role in the tested samples. Dispersion of ceramic particles should also be considered, as is used e.g., in oxide strengthening steels (ODS). Although the samples contained oxide and nitride particles, the size of these particles in all samples is equivalent, as shown in Table 2. Consequently, the particles are not expected to change the hardness between the samples significantly. Additionally, the formation of secondary phases also affects the hardness. Thus, the mechanisms to increase the hardness from 2Ti-mix-N2 as a base material are discussed from the viewpoints of strengthening by grain refinement, solid solution strengthening, and secondary phase formation.

As shown in Table 4, the material 2Ti-mix-N2 has the lowest hardness. The hardness increases with the increase of the Ti content in the mixture samples. Fe_2Ti Laves phase was found in 7.5Ti-mix-N2. Since Laves phase can be used as strengthening secondary phase in ferritic steels [57], the hard Laves phase, Fe_2Ti, likely contributed to the hardness increase of 7.5Ti-mix-N2 sample. However, from an application standpoint, the presence of (Laves) grain boundary phase is expected to lead to undesired embrittlement.

The effect of grain refinement becomes apparent by comparing the two alloyed samples, 5Ti-alloyed-Ar and 5Ti-alloyed-N2, of similar chemical composition (except N contents). Because Ti binds N in 5Ti-alloyed-N2, it can be assumed that the difference in grain size is the main reason for the difference in hardness between these two samples (41.4 HV). As shown in Fig. 7 (d) and (e), the 5Ti-alloyed-Ar contained coarser grains than the 5Ti-alloyed-N2, which results in the higher hardness of the latter sample. Because of the bimodal grain distribution of 5Ti-alloyed-Ar and the intense texture of 2Ti-mix-N2, the Hall-Petch law parameters cannot be obtained from the current results.

The effect of grain refinement on the 0.2% proof stress in both samples is estimated to be around 118 MPa by the correlation formula proposed by Pavlina et al. [58]. A combination of high tensile strength and elongation was experimentally found for ferritic stainless steel, consisting of equiaxed grains with fine hard particles [34]. Thus, it is estimated that grain refinement by the dispersion of Ti(O,N) particles is a practical strengthening method for ferritic steels.

The 5Ti-mix-N2, 5Ti-mix-Ar, and 5Ti-alloyed-N2 samples show fine equiaxed grains as shown in Fig. 8, and all average grain diameters are almost equivalent. Although the 2Ti-mix-N2 shows coarse grains, the anisotropic grain shape and ⟨0 0 1⟩ texture prevent us from estimating the Hall-Petch parameters.

Because the 5Ti-mix-N2 and 5Ti-alloyed-N2 samples exhibited similar grain size distributions, as shown in Table 2, the solid solution strengthening effect by Ti solute can be identified using the clear difference in hardness between both samples. Despite the same nominal Ti content, the actual Ti content in the LPBF-built sample 5Ti-mix-N2 was lower than 5 at.% (Table 3). If the hardness variation is caused by the Ti content, the effect of the Ti content was roughly 27 HV/at.% (Table 4). This result indicates that the solid solution strengthening of Ti is not negligible, which is consistent with the effect of substitutional elements investigated by Jiang et al. [59].

4.6. Benefits of grain refinement by the in-situ formation of TiO and Ti(O,N)

As discussed in the previous sections, the grain refinement of Fe–Ti alloys was achieved by the formation of particles having the B–N OR with ferrite. The mechanisms of the formation are (a) in-situ formation of TiO by the reaction between the melt pool and O in the raw powders, (b) in-situ formation of Ti(O,N) by the reaction between the molten metals and N_2 gas, and (c) the direct addition (mixing) of the TiN particles. Thus, both the in-situ formation and ex-situ addition of particles led to grain refinement, proposing a new concept for the alloy and powder development for LPBF.

The usage of ex-situ added fine ceramic powders in LPBF has severe drawbacks. For example, it has been limited in quantity, or laborious processes such as coating [30,31] have been required, because even a small amount of the ceramic particles strongly deteriorates the powder mixture's flowability. We could observe the same effect in our study. In contrast, the in-situ method promoted grain refinement without mixing Ti ceramics particles, maintaining the powder flowability. Additionally, adding relatively large amounts of high-melting ceramic particles always carries the risk of the formation of large agglomerates, which can lead to stress-concentrating defects in the final material, thus deteriorating its fracture toughness and fatigue resistance. By the in-situ formation of the inoculating particles, this problem is strongly reduced.

Another problem for the ex-situ method is finding a suitable set of laser parameters for LPBF because of the difference in melting temperatures and laser absorptivity between the metal and ceramic particles. An inadequate laser energy density can lead to the incomplete reaction between the metallic matrix and ceramic particles, resulting in a low density or unreacted interface between the matrix and particle. For example, the specimens with added TiN particles could not be fabricated using low laser energy density because of the formation of the unreacted interfaces. In the case of in-situ formation, only mixing of different metallic matrix powders occurs, so relatively large variations of the laser conditions are possible.

Ti(O,N) and TiN particles have been widely used as inoculants for ferritic stainless steels to promote equiaxed grains [36], and the effectiveness of the particles in LPBF was confirmed in this study. Additionally, we show that thermodynamic calculations can predict which primary particles form. Together with the ability to calculate the misfit strain of the B–N OR, this allows to predict under which circumstances grain refinement can be expected or not. Thus, our approach has broad applicability for the entire alloy class of ferritic steels. For example, we confirmed that adding 5 at.%Ti to AISI 430 ferritic steel (Fe-17 at.%Cr) realized fine grains in the previous work [33]. The availability of this mechanism for refinement is strongly beneficial, because other mechanisms like eutectic solidification (as applied e.g., in Al–Si [27] and Ti–Cu [28] alloys) cannot be applied to stainless steels.

5. Conclusions

We investigated the microstructures of ferritic Fe–Ti steels fabricated by laser powder bed fusion (LPBF). The microstructures of the samples built with powder mixtures of pure Fe and Ti powders, and alloyed Fe-5at.%Ti powder were compared. The effect of TiN powder addition to the Fe-2at.%Ti powder mixture was also investigated.

(1) Fe-2at.%Ti fabricated by the LPBF using pure Fe and Ti powder mixture formed coarse columnar grains oriented along the building direction. The texture shows a strong ⟨0 0 1⟩ component in the building direction.
(2) In contrast, powder mixtures of Fe-5at.%Ti and Fe-7.5at.%Ti showed very strong grain refinement and a random texture. Mostly spherical sub-micron-sized particles were observed in all samples. EBSD and TEM analysis as well as thermodynamic calculations revealed that the particles for Fe-2at.%Ti and Fe-5at.%Ti powder mixtures are Ti_2O_3 and TiO, respectively. The source of O in these cases was due to the high O content in the raw Fe powder. Only the TiO particles acted as heterogeneous nucleation sites for ferrite and hence as effective grain refiners due to the small lattice misfit with ferrite. A similar effect was found for the addition of 2 vol% of TiN particles, which also resulted in fine equiaxed grains for the Fe-2at.%Ti power mixture.
(3) The grain refinement behavior of Fe-5at.% Ti powder mixture samples was not affected by the building atmosphere (Ar or N_2), because there is sufficient TiO formed from O in the raw powder for effective grain refinement in both atmospheres. However, the sample using the Fe-5at.%Ti alloyed powder showed fine grains only when it was built under N_2 atmosphere. This behavior was caused by Ti(O,N) particle formation via reactions between the melt pool and N_2 gas.
(4) The grain refinement increased the Vickers hardness as predicted by the Hall-Petch relationship. Additionally, solid solution strengthening by Ti was found.

Funding

This research did not receive any specific grant from funding agencies in the public, commercial, or not-for-profit sectors.

Declaration of Competing Interest

The authors declare that they have no known competing financial interests or personal relationships that could have appeared to influence the work reported in this paper.

Appendix A

Greenwald et al. estimated the thermal distribution ($T(z,t)$), thermal gradient ($G(z,t)$), and heating/cooling rate ($R(z,t)$) developed by laser illumination using the following eq. (A-1) [46];

$$T(z,t)=\frac{q}{k}\left[\sqrt{\frac{4\alpha t}{\pi}}e^{-\left(\frac{z}{\sqrt{4\alpha t}}\right)^2}-\sqrt{\frac{4\alpha(t-\tau)}{\pi}}e^{-\left(\frac{z}{\sqrt{4\alpha(t-\tau)}}\right)^2}-z\left\{erfc\left(\frac{z}{\sqrt{4\alpha t}}\right)-erfc\left(\frac{z}{\sqrt{4\alpha(t-\tau)}}\right)\right\}\right]+T_0 \quad (A-1)$$

$$G(z,t)=-\frac{q}{k}\left[erfc\left(\frac{z}{\sqrt{4\alpha t}}\right)-erfc\left(\frac{z}{\sqrt{4\alpha(t-\tau)}}\right)\right] \quad (A-2)$$

$$R(z,t)=\frac{q}{k}\left[\sqrt{\frac{\alpha}{\pi t}}e^{-\left(\frac{z}{\sqrt{4\alpha t}}\right)^2}-\sqrt{\frac{\alpha}{\pi(t-\tau)}}e^{-\left(\frac{z}{\sqrt{4\alpha(t-\tau)}}\right)^2}\right] \quad (A-3)$$

where T is temperature, T_0 is the initial temperature, z is the depth from the surface, t is time, q is the absorbed laser power density, α is the laser absorptivity, κ is the thermal conductivity, ρ is the material density, c is the specific heat capacity, and τ is the heating time. Although eqs. (A-1)–(A-3) were established under the assumption of materials with high thermal conductivities, the equations can be applicable to the evaluation of relative thermal conditions [60]. The interfacial moving velocity ($V(z,t)$) is obtained from eq. A-(4), using the eqs. (A-2) and (A-3).

$$V(z,t) = \frac{R(z,t)}{G(z,t)} \quad (A-4)$$

The building conditions (e.g., the laser power density) of all samples were the same, so the calculation results of the equations depend on the thermal properties. We applied the pure iron density for the material density, c, and the ambient temperature was estimated at 500 K. Peet et al. proposed the prediction model of the thermal conductivity for Fe based alloys [61]. Their results prospected that the thermal conductivity of low alloy steels was not affected by the chemical composition around melting points. The specific heat capacities, c were calculated by thermodynamic calculation. The laser absorptivity of a powder mixture was obtained from the mixing theory. The laser absorption coefficients of the pure Fe and Ti atomized powders were reported to be 0.64 and 0.77 at the wavelength of 1070 nm, respectively [62]. By using the estimated values shown in Table A-1, the calculations of the thermal gradients (G), the cooling rates (R), and interfacial moving velocity (V) were carried out at the position where $T = T_m$ (T_m: melting temperature calculated by Thermo-Calc), and $z = 40$ μm (the layer thickness). All parameters used to calculate the result shown in Table 5 were displayed in Table A-1.

Table A-1
Parameters used for the thermal distribution calculations.

composition	Laser absorptivity	Thermal conductivity	Specific heat capacity	Melting temperature	Ambient temperature	Density
		W/mK	J/gK	K	K	g/cm^3
Fe-2at.%Ti	0.644	32.45	0.735	1783	500	7.83
Fe-5at.%Ti	0.650	32.68	0.727	1743	500	7.75
Fe-7.5at.%Ti	0.654	33.05	0.720	1708	500	7.69

References

[1] P. Bajaj, A. Hariharan, A. Kini, P. Kürnsteiner, D. Raabe, E.A. Jägle, Steels in additive manufacturing: a review of their microstructure and properties, Mater. Sci. Eng. A 772 (2020) 138633.

[2] H. Zhang, H. Zhu, X. Nie, J. Yin, Z. Hu, X. Zeng, Effect of Zirconium addition on crack, microstructure and mechanical behavior of selective laser melted Al-Cu-Mg alloys, Scr. Mater. 134 (2017) 6–10.

[3] R. Li, M. Wang, Z. Li, P. Cao, T. Yuan, H. Zhu, Developing a high-strength Al-Mg-Si-Sc-Zr alloy for selective laser melting: crack-inhibiting and multiple strengthening mechanisms, Acta Mater. 193 (2020) 83–98.

[4] L. Thijs, K. Kempen, J.-P. Kruth, J.V. Humbeeck, Fine-structured aluminium products with controllable texture by selective laser melting of pre-alloyed AlSi10Mg powder, Acta Mater. 61 (2013) 1809–1819.

[5] W. Shifeng, L. Shuai, W. Qingsong, C. Yan, Z. Sheng, S. Yusheng, Effect of molten pool boundaries on the mechanical properties of selective laser melting parts, J. Mater. Process. Technol. 214 (2014) 2660–2667.

[6] K.N. Amat, S.M. Gaytan, L.E. Murr, E. Martinez, P.W. Shindo, J. Hernande, S. Collins, F. Medina, Microstructures and mechanical behavior of Inconel 718 fabricated by selective laser melting, Acta Mater. 60 (2012) 2229–2239.

[7] B. Song, S. Dong, P. Coddet, H. Liao, C. Coddet, Fabrication of NiCr alloy parts by selective laser melting: columnar microstructure and anisotropic mechanical behavior, Mater. Des. 53 (2014) 1–7.

[8] T. Boegelein, S.N. Dryepondt, A. Pandey, K. Dawson, G.J. Tatlock, Mechanical response and deformation mechanisms of ferritic oxide dispersion strengthened steel structures produced by selective laser melting, Acta Mater. 87 (2015) 201–215.

[9] L. Thijs, M.L.M. Sistiaga, R. Wauthle, Q. Xie, J.-P. Kruth, J.V. Humbeeck, Strong morphological and crystallographic texture and resulting yield strength anisotropy in selective laser melted tantalum, Acta Mater. 61 (2013) 4657–4668.

[10] K.V. Yang, Y. Shi, F. Palm, X. Wu, P. Rometsch, Columnar to equiaxed transition in Al-Mg(-Sc)-Zr alloys produced by selective laser melting, Scr. Mater. 145 (2018) 113–117.

[11] Q. Zhang, J. Chen, X. Lin, H. Tan, W.D. Huang, Grain morphology control and texture characterization of laser solid formed Ti6Al2Sn2Zr3Mo1.5Cr2Nb titanium alloy, J. Mater. Process. Technol. 238 (2016) 202–211.

[12] B. AlMangour, D. Grzesiak, T. Borkar, J.-M. Yang, Densification behavior, microstructural evolution, and mechanical properties of TiC/316L stainless steel nanocomposites fabricated by selective laser melting, Mater. Des. 138 (2018) 119–128.

[13] S. Liu, H. Zhu, G. Peng, J. Yin, X. Zeng, Microstructure prediction of selective laser melting AlSi10Mg using finite element analysis, Mater. Des. 142 (2018) 319–328.

[14] R.R. Dehoff, M.M. Kirka, W.J. Sames, H. Bilheux, A.S. Tremsin, L.E. Lowe, S.S. Babu, Site specific control of crystallographic grain orientation through electron beam additive manufacturing, Mater. Sci. Technol. 31 (2015) 931–938.

[15] H.Y. Wan, Z.J. Zhou, C.P. Li, G.F. Chen, G.P. Zhang, Effect of scanning strategy on grain structure and crystallographic texture of Inconel 718 processed by selective laser melting, J. Mater. Sci. Technol. 34 (2018) 1799–1804.

[16] B. AlMangour, D. Grzesiak, J.-M. Yang, Scanning strategies for texture and anisotropy tailoring during selective laser melting of TiC/316L stainless steel nanocomposites, J. Alloys Compd. 728 (2017) 424–435.

[17] W. Xiong, L. Hao, Y. Li, D. Tang, Q. Cui, Z. Feng, C. Yan, Effect of selective laser melting parameters on morphology, microstructure, densification and mechanical properties of supersaturated silver alloy, Mater. Des. 170 (2019) 107697.

[18] R. Shi, S.A. Khairallah, T.T. Roehling, T.W. Heo, J.T. McKeown, M.J. Matthews, Microstructural control in metal laser powder bed fusion additive manufacturing using laser beam shaping strategy, Acta Mater. 184 (2020) 284–305.

[19] T.T. Roehling, R. Shi, S.A. Khairallah, J.D. Roehling, G.M. Guss, J.T. McKeown, M.J. Matthews, Controlling grain nucleation and morphology by laser beam shaping in metal additive manufacturing, Mater. Des. 195 (2020) 109071.

[20] T.D. McLouth, G.E. Bean, D.B. Witkin, S.D. Sitzman, P.M. Adams, D.N. Patel, W. Park, J.-M. Yang, R.J. Zaldivar, The effect of laser focus shift on microstructural variation of Inconel 718 produced by selective laser melting, Mater. Des. 149 (2018) 205–213.

[21] Y.S. Lee, M.M. Kirka, R.B. Dinwiddie, N. Raghavan, J. Turner, R.R. Dehoff, S.S. Babu, Role of scan strategies on thermal gradient and solidification rate in electron beam powder bed fusion, Addit. Manufact. 22 (2018) 516–527.

[22] D. Zhang, D. Qiu, S. Zhu, M. Dargusch, D. StJohn, M. Easton, Grain refinement in laser remelted Mg-3Nd-1Gd-0.5Zr alloy, Scr. Mater. 183 (2020) 12–16.

[23] D. Zhang, D. Qiu, M.A. Gibson, Y. Zheng, H.L. Fraser, A. Prasad, D.H. StJohn, M.A. Easton, Refining prior-β grains of Ti–6Al–4V alloy through yttrium addition, J. Alloys Compd. 841 (2020) 155733.

[24] A. Prasad, L. Yuan, P. Lee, M. Patel, D. Qiu, M. Easton, D. StJohn, Towards understanding grain nucleation under additive manufacturing solidification conditions, Acta Mater. 195 (2020) 392–403.

[25] Y. Li, D. Gu, Thermal behavior during selective laser melting of commercially pure titanium powder: numerical simulation and experimental study, Addit. Manufact. 1–4 (2014) 99–109.

[26] D. Zhang, A. Prasad, M.J. Bermingham, C.J. Todaro, Michael J. Benoit, Mitesh N. Patel, Dong Qiu, David H. StJohn, Ma Qian, Mark A. Easton, Grain refinement of alloys in fusion-based additive manufacturing processes, Metall. Mater. Trans. A 51 (2020) 4341–4359.

[27] M.L. Montero-Sistiaga, R. Mertens, B. Vrancken, X. Wang, B.V. Hooreweder, J.P. Kruth, J.B. Humbeeck, Changing the alloy composition of Al7075 for better processability by selective laser melting, J. Mater. Process. Technol. 238 (2016) 437–445.

[28] D. Zhang, D. Qiu, M.A. Gibson, Y. Zheng, H.L. Fraser, D.H. StJohn, M.A. Easton, Additive manufacturing of ultrafine-grained high-strength titanium alloys, Nature 576 (2019) 91–95.

[29] R. Li, M. Wang, T. Yuan, B. Song, C. Chen, K. Zhou, P. Cao, Selective laser melting of a novel Sc and Zr modified Al-6.2 Mg alloy: processing, microstructure, and properties, Powder Technol. 319 (2017) 117–128.

[30] J.H. Martin, B.D. Yahata, J.M. Hundley, J.A. Mayer, T.A. Schaedler, T.M. Pollock, 3D printing of high-strength aluminium alloys, Nature 549 (2017) 365–369.

[31] J.H. Martin, B. Yahata, J. Mayer, R. Monea, E. Stonkevitch, J. Millera, M.R. O'Masta, T. Schaedler, J. Hundley, P. Callahan, T. Pollock, Grain refinement mechanisms in additively manufactured nano-functionalized aluminum, Acta Mater. 200 (2020) 1022–1037.

[32] M.J. Bermingham, D.H. StJohn, J. Krynen, S. Tedman-Jones, M.S. Dargusch, Promoting the columnar to equiaxed transition and grain refinement of titanium alloys during additive manufacturing, Acta Mater. 168 (2019) 261–274.
[33] H. Ikehata, E. Jägle, Grain refinement of Fe-X alloys fabricated by laser powder bed fusion, Mater. Sci. Forum 1016 (2021) 580–586.
[34] D. Karlsson, C.Y. Chou, N.H. Pettersson, T. Helander, P. Harlin, M. Sahlberg, G. Lindwall, J. Odqvist, U. Jansson, Additive manufacturing of the ferritic stainless steel SS441, Addit. Manufact. 36 (2020) 101580.
[35] A. Durga, N.H. Pettersson, S.B.A. Malladi, Z. Chen, S. Guo, L. Nyborg, G. Lindwall, Grain refinement in additively manufactured ferritic stainless steel by in situ inoculation using pre-alloyed powder, Scr. Mater. 194 (2021) 113690.
[36] J.H. Park, Y.J. Kang, Inclusions in stainless steels — A review, Steel Res. Int. 88 (2017) 1700130.
[37] V. Villaret, F. Deschaux-Beaume, C. Bordreuil, S. Rouquette, C. Chovet, Influence of filler wire composition on weld microstructures of a 444 ferritic stainless steel grade, J. Mater. Process. Technol. 213 (2013) 1538–1547.
[38] V. Villaret, F. Deschaux-Beaume, C. Bordreuil, A solidification model for the columnar to equiaxed transition in welding of a Cr-Mo ferritic stainless steel with Ti as inoculant, J. Mater. Process. Technol. 233 (2016) 115–124.
[39] X. Gan, Q. Yuan, G. Zhao, H. Ma, W. Liang, Z. Xue, W. Qiao, G. Xu, Quantitative analysis of microstructures and strength of Nb-Ti microalloyed steel with different Ti additions, Metall. Mater. Trans. A 51 (2020) 2084–2096.
[40] L.S. Aota, P. Bajaj, H.R.Z. Sandim, E.A. Jägle, Laser powder-bed fusion as an alloy development tool: parameter selection for in-situ alloying using elemental powders, Materials 13 (2020) 3922.
[41] J.A. Dantzig, M. Rappaz, Solidfication, 2nd edition EPFL Press, 2016 (Chapter 7).
[42] Z.G. Yang, M. Enomoto, Discrete lattice plane analysis of baker-nutting related B1 compound/ferrite interfacial energy, Mater. Sci. Eng. A 332 (2002) 184–192.
[43] J.D. Hunt, Steady state columnar and equiaxed growth of dendrites and eutectic, Mater. Sci. Eng. 65 (1984) 75–83.
[44] M.A. Martorano, C. Beckermann, C.-A. Gandin, A solutal interaction mechanism for the columnar-to-equiaxed transition in alloy solidification, Metall. Mater. Trans. A 34A (2003) 1657–1674.
[45] M. Gäumann, R. Trivedi, T.V. Kurz, Nucleation ahead of the advancing interface in directional solidification, M. Gaumann, Mater. Sci. Eng. A 226-228 (1997) 763–769.
[46] L.E. Greenwald, E.M. Breinan, B.H. Kear, Heat transfer properties and microstructures of laser surface melted alloys, AIP Conf. Proc. 50 (189) (1979) 189–204.
[47] B.L. Bramfitt, The effect of carbide and nitride additions on the heterogeneous nucleation behavior of liquid iron, Metall. Trans. A. 1 (1988) 1970–1987.
[48] H. Suito, H. Ohta, S. Morioka, Refinement of solidification microstructure and austenite grain by fine inclusion particles, ISIJ Int. 46 (2006) 840–846.
[49] M. Simonelli, C. Tuck, N.T. Aboulkhair, I. Maskery, I. Ashcroft, R.D. Wildman, R. Hague, A study on the laser spatter and the oxidation reactions during selective laser melting of 316L stainless steel, Al-Si10-Mg, and Ti-6Al-4V, Metall. Mater. Trans. A 46 (2015) 3842–3851.
[50] Y. Liu, Y. Yang, S. Mai, D. Wang, C. Song, Investigation into spatter behavior during selective laser melting of AISI 316L stainless steel powder, Mater. Des. 87 (2015) 797–806.
[51] H. Springer, C. Baron, A. Szczepaniak, E.A. Jägle, M.B. Wilms, A. Weisheit, D. Raabe, Efficient additive manufacturing production of oxide- and nitride-dispersion-strengthened materials through atmospheric reactions in liquid metal deposition, Mater. Des. 111 (2016) 60–69.
[52] L. Thijs, J. Van Humbeeck, K. Kempen, E. Yasa, J.P. Kruth, M. Rombouts, Investigation on the Inclusions in Maraging Steel Produced by Selective Laser Melting, Innovative Developments in Virtual and Physical Prototyping, Batrolo et al. (eds), Taylor & Fancis Group, London, 2012, ISBN 978-0-415-68418-7 297–304.
[53] H. Yang, P.G. McCormick, Synthesis of titanium oxynitride by mechanical milling, J. Mater. Sci. 28 (1993) 5663–5667.
[54] X. Liu, C. Zhao, X. Zhou, Z. Shen, W. Liu, Microstructure of selective laser melted AlSi10Mg alloy, materials and design, Mater. Des. 168 (2019) 107677.
[55] D. Akama, N. Nakada, T. Tsuchiyama, S. Takaki, A. Hironaka, Discontinuous yielding induced by the addition of nickel to interstitial-free steel, Scr. Mater. 82 (2014) 13–16.
[56] K. Takeda, N. Nakada, T. Tsuchiyama, S. Takaki, Effect of interstitial elements on Hall–Petch coefficient of ferritic Iron, ISIJ Int. 48 (2008) 1122–1125.
[57] F. Löffler, M. Palm, G. Sauthoff, Iron-rich iron-titanium-silicon alloys with strengthening intermetallic laves phase precipitates, Steel Res. Int. 5 (2004) 766–772.
[58] E.J. Pavlina, C.J. VVan Tyne, Correlation of yield strength and tensile strength with hardness for steels, J. Mater. Eng. Perform. 17 (2008) 888–893.
[59] F. Jiang, T. Masumura, T. Tsuchiyama, S. Takaki, Effect of substitutional element addition on Hall-Petch relationship in interstitial free ferritic steels, ISIJ Int. 59 (2019) 1929–1931.
[60] P. Bajaj, J. Wright, I. Todd, E.A. Jägle, Predictive process parameter selection for selective laser melting manufacturing: applications to high thermal conductivity alloys, Addit. Manufact. 27 (2019) 246–258.
[61] M.J. Peet, H.S. Hasan, H.K.D.H. Bhadeshia, Prediction of thermal conductivity of steel, Int. J. Heat Mass Transf. 54 (2011) 2602–2608.
[62] N.K. Tolochko, T. Laoui, Y.V. Khlopkov, S.E. Mozzharov, V.I. Titov, M.B. Ignatiev, Absorptance of powder materials suitable for laser sintering, Tolochko Rapid Prototyping J. 6 (2000) 155–160.